

## Spatially resolved acoustic spectroscopy for rapid imaging of material microstructure and grain orientation

This content has been downloaded from IOPscience. Please scroll down to see the full text.

2014 Meas. Sci. Technol. 25 055902

(<http://iopscience.iop.org/0957-0233/25/5/055902>)

View [the table of contents for this issue](#), or go to the [journal homepage](#) for more

### Download details:

This content was downloaded by: eexrjs

IP Address: 128.243.74.2

This content was downloaded on 04/04/2014 at 06:56

Please note that [terms and conditions apply](#).

# Spatially resolved acoustic spectroscopy for rapid imaging of material microstructure and grain orientation

**Richard J Smith, Wenqi Li, Jethro Coulson, Matt Clark, Michael G Somekh and Steve D Sharples**

Electrical Systems and Optics Research Division, University of Nottingham, University Park, Nottingham, NG7 2RD, UK

E-mail: [Richard.j.smith@nottingham.ac.uk](mailto:Richard.j.smith@nottingham.ac.uk)

Received 29 November 2013, revised 14 January 2014

Accepted for publication 17 January 2014

Published 14 March 2014

## Abstract

Measuring the grain structure of aerospace materials is very important to understand their mechanical properties and in-service performance. Spatially resolved acoustic spectroscopy is an acoustic technique utilizing surface acoustic waves to map the grain structure of a material. When combined with measurements in multiple acoustic propagation directions, the grain orientation can be obtained by fitting the velocity surface to a model. The new instrument presented here can take thousands of acoustic velocity measurements per second. The spatial and velocity resolution can be adjusted by simple modification to the system; this is discussed in detail by comparison of theoretical expectations with experimental data.

Keywords: surface acoustic waves, material characterization, laser ultrasound, grain orientation

(Some figures may appear in colour only in the online journal)

## 1. Introduction


Imaging and measuring the microstructure of aerospace materials is becoming more important as the materials are pushed ever closer to their working limits. Small changes to the grain structure or orientation can have a large effect on the performance of the material, for example, small changes to the primary and secondary angles of a single crystal turbine blade [1] can lead to different stress responses for the same loading conditions, potentially impacting the fatigue life of the blade [2]. For multigrain materials, the size [3, 4] and distribution [5] of grains play an important role in determining the mechanical properties of the material.

The orientation of grains in a material is especially important for certain types of alloys that are susceptible to dwell fatigue [6, 7], of which one contributing factor is the presence of rogue grain combinations in the loading direction leading to premature failure of the material [8, 9].

Welding [10] of materials leads to growth of grains as the material cools leading to substantial differences in the grain structure and hence material properties at the weld compared to the bulk material. Understanding the evolution of the change in grain structure is important for understanding the strength of these bonds [11], and how ultrasonic bulk waves interact with the weld microstructure in non-destructive evaluation (NDE) applications.

Additive manufacturing techniques, such as direct laser deposition [12] and arc weld deposition [13], are being increasingly used to manufacture aerospace components. These techniques have the potential to have a large impact on manufacturing costs. The ability to make very complex single parts is very advantageous, but for safety critical components the performance of the material must be ensured and this means that the grain structure needs to be known [14]. This requires non-destructive measurement of the grain structure on the final part.

Working of material, both hot and cold, can have an impact on the grain structure. This leads to the need to monitor the grain structure from production of the raw material through to the final part as changes to the grain structure whilst working

 Content from this work may be used under the terms of the [Creative Commons Attribution 3.0 licence](https://creativecommons.org/licenses/by/3.0/). Any further distribution of this work must maintain attribution to the author(s) and the title of the work, journal citation and DOI.

the material to make the component could have significant implications for its durability [15, 16].

There are a number of techniques employed for imaging the grain structure of materials; these are split into two main groups, techniques that provide contrast images of grain structure and others that provide grain orientation measurements.

Chemical etching [17] and optical microscopy techniques [18] produce images that show the material microstructure, but the orientation of the grains is not determined so there is a possibility for grains of differing orientation to appear the same optically. Analysis of the images is somewhat subjective, due to the qualitative nature of the information revealed by optical contrast; however, the contrast maps produced by these techniques are very useful for estimating the grain size and texture of the material; they can be performed on large parts and relatively quickly, although in the case of etching there are additional processing steps that the part has to go through which adds to the cost and time of inspection.

Grain orientation can be obtained directly using x-ray or electron microscopy techniques. The most common x-ray technique is Laue diffraction [19]; there an x-ray source is directed at a sample and either the back reflected or the transmission diffraction pattern is recorded. Analysis of the shape of the pattern allows the crystallographic orientation to be obtained. The main drawback of this technique is the comparatively low spatial resolution ( $\sim 1$  mm for standard systems, although it can be  $\sim 10$   $\mu\text{m}$  for speciality  $\mu\text{XRD}$  systems) which means it is typically used for materials with very large grains or those which are nominally single crystals (e.g. single crystal nickel super alloy [1, 2]). Also, a trained operator is required to manually match the measured diffraction pattern to a pattern of known orientation. Electron backscatter diffraction (EBSD) [20] provides very high spatial resolution and high accuracy of the grain orientation by analysis of the diffraction patterns obtained from an electron source diffracting off the crystal lattice of the sample. The main drawbacks of EBSD are the limited size of the sample that can be imaged—typically less than  $20 \times 20$   $\text{mm}^2$  (small enough to fit in an SEM vacuum chamber) and the exacting surface preparation required e.g. requiring a mirror like polish without a significant oxide layer is required in order to achieve good orientation measurements. For most practical engineering samples, this essentially becomes a destructive technique as the part itself cannot be imaged without being cut up.

We have developed an instrument around an acoustic technique that can perform similar grain orientation measurements, on samples of any size and varying degrees of surface finish, albeit with a lower spatial resolution (tens of microns) than obtained by electron microscopy techniques.

Although the spatially resolved acoustic spectroscopy technique has been described previously [21], the new instrument uses a different approach which has led to a step change in performance and a large reduction in the overall instrument size. This paper also discusses the velocity and spatial resolution in detail comparing theoretical expectations with those obtained from experimental measurements.

The spatially resolved acoustic spectroscopy technique is analogous to optical spectroscopy techniques where analysis

of the optical spectrum and the wavelengths that are most readily transmitted or absorbed tells us some properties of the sample being examined. In our acoustic case, we monitor the spectrum of sound waves emitted from a grating source, by either looking at the generation efficiency of a fixed frequency laser as the grating period is swept or by analysing the frequencies generated by a broadband laser source through a fixed period grating. Previous systems used the first approach which is inherently slow due to the requirement to sweep the grating spacing, therefore requiring multiple measurements to establish the acoustic velocity of the sample.

The new instrument uses the second approach as the surface acoustic wave (SAW) velocity can be obtained in a single measurement. To measure the acoustic spectrum at each point on the sample, a fixed grating is illuminated with a short laser pulse. As the laser pulse contains a broad range of frequencies, the frequencies which match the grating spacing and acoustic velocity of that sample point will be generated with optimum efficiency. We measure the waves that have been generated close to the excitation region. We can then calculate the frequencies generated ( $f$ ), and with the knowledge of the grating spacing ( $\lambda$ ) we can obtain the acoustic velocity ( $v$ ) using  $v = f\lambda$ . To build up a velocity map, the sample is raster scanned and the measurement is repeated for each point.

The instrument and its capabilities will now be described in more detail.

## 2. The instrument

The SRAS instrument is built around a compact Q-switched laser from AOT lasers (AOT-YAG-10Q). This laser provides 1–2 ns pulses with pulse energies of 50–150  $\mu\text{J}$  at a repetition rate of 1–12.5 kHz. The short laser pulses allow a wide operating range for the generation of the acoustic waves from the low MHz to high 100 s of MHz. The breadth of this source allows the instrument to be flexible in terms of spatial and velocity resolution as discussed later in section 5.

The optical arrangement of the system is shown in figure 1. The Q-switched laser is used to illuminate an optical mask. The mask is a chromium pattern on a fused quartz substrate manufactured by JD Photo Ltd; this pattern is imaged to the sample surface. The line spacing and magnification of the imaging system determine the wavelength of the acoustic waves that will be generated. Typically, we use a 5:1 reduction to the sample surface using a long working distance objective lens (Mitutoyo M plan APO  $\times 10$ , focal length 20 mm) and a tube lens with focal length of 100 mm. The optical mask has an aperture that is typically varied between 0.3 and 1 mm, and so after being reimaged to the sample surface the generation patch size is between 60 and 200  $\mu\text{m}$ . Figure 2 shows the projected fringe pattern on the sample surface as viewed by the CMOS camera imaging arm (not shown in schematic).

The detection laser is a fibre coupled 532 nm continuous wave laser with an output power of  $\sim 200$  mW (Laser Quantum Torus 532). The beam passes through a polarizing beam splitter (PBS) and quarter wave plate before being combined with the generation path by a dichroic mirror which reflects 532 nm light and transmits 1064 nm (Laser Components); it is then

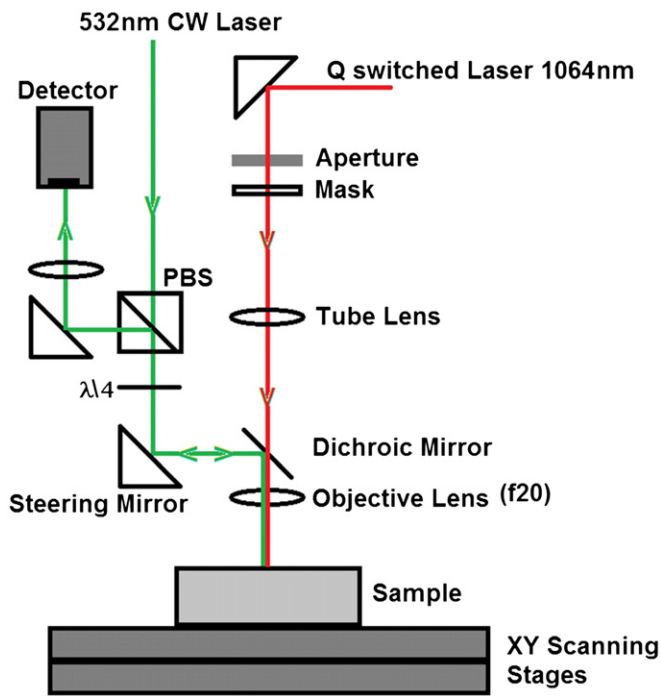


Figure 1. The optical configuration used by the new instrument.

focused to the sample through the same imaging lens as the generation laser. The focal spot diameter is approximately  $8\ \mu\text{m}$  and positioned to the side of the generation region as shown in figure 2. The position of the spot on the sample is controlled by a computer controllable piezoelectric steering mirror (Newport Agilis AG-M100L) that allows the adjustment of the input angle of the detection beam to the objective lens.

The returning beam from the sample surface retraces the same path back through the system, and passes through the quarter wave plate again; this causes the polarization to be flipped by  $90^\circ$  with respect to the input beam and the detection laser is now reflected by the PBS and is directed to the final lens of the system focusing the beam just beyond the split photodiode detector.

The  $8\ \mu\text{m}$  probe beam spot size sets a limit to the minimum wavelength of the projected fringes; if the spot size is larger than half the acoustic wavelength, then the detection efficiency is significantly reduced [22] and to work beyond this requires reducing the spot size by increasing the numerical aperture of the objective lens.

The SRAS system could use a number of different types of detectors, sensitive to surface displacement or optical beam deflection, depending on the range of expected frequencies and the surface finish of the sample. For samples with strong specular reflections, the detector used is a knife edge detector, based on the principle of optical beam deflection; this is sensitive to the out-of-plane surface motion in one propagation direction. As the acoustic waves pass under the probe beam spot, it causes the beam to be deflected and if this motion is across the split photodiode we measure the presence of the propagating waves. The output of the detector is then amplified and band pass filtered and the trace is recorded on a digital oscilloscope (Lecroy, Wavemaster 64Xi).

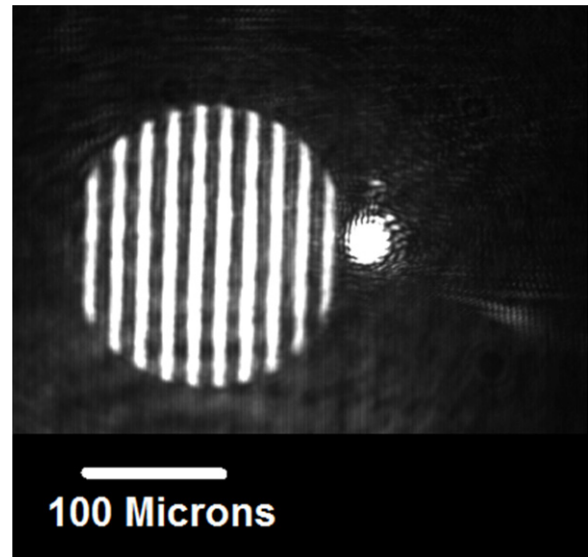


Figure 2. Example image of the projected fringes on the sample surface; in this case, the line spacing is approximately  $19\ \mu\text{m}$  and the total patch size is  $200\ \mu\text{m}$ .

To obtain fast scanning rates, we record the signal each time the laser fires. This requires scanning on the fly and saving all traces for the scan line in the oscilloscope's segmented memory, which guarantees acquisition for every trigger event. The registration of each data point with the scanning stages is achieved by ensuring that the stage velocity is constant over the scan range. To do this, we trigger the scope with a gated version of the laser pulse train so that the scope will only acquire data after the start point of the scan; sufficient acceleration distance is allowed to ensure the stages are moving at a constant velocity before reaching the start point. This ensures that we know where the position of each measurement point on the sample.

The use of compact lasers and fibre optics means that the optical head only occupies a volume of approximately  $350 \times 200 \times 150\ \text{mm}^3$  with an umbilical to an equipment rack containing the laser power supplies, electronics and PC (as shown in figure 3).

A number of features of the system will now be discussed and illustrated by images of a number of different materials taken with the instrument.

### 3. Scanning speed and sample size

The SRAS instrument is capable of scanning large samples quickly, due to the high speed acquisition system. The acoustic data are recorded for each laser pulse, typically 6250 times per second. In the current instrument, there are a number of overheads in the acquisition system that reduces the overall scan rate to around 1000 points per second. This is primarily due to the oscilloscope used to acquire the data and to remove this bottle neck we are designing a custom data acquisition system. Ultimately, the acquisition speed is limited by the maximum repetition rate of the laser.

Figure 4 shows scans of two samples with diameters of 95 and 105 mm; the 7.5 mega pixel images took  $\sim 2.5\ \text{h}$  to obtain. Figures 4(A) and (B) are example images of Ti-6Al-4V billets taken with the SRAS instrument. Image A shows

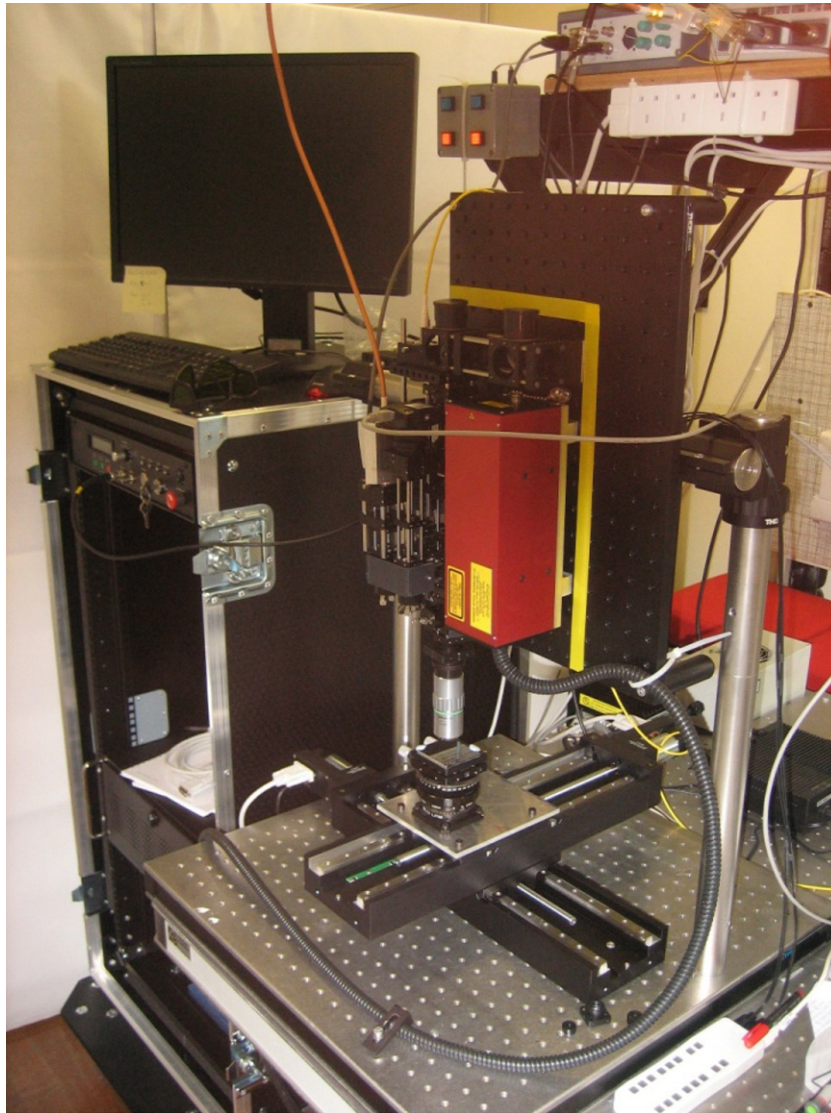


**Figure 3.** Photograph of the current instrument showing the head and electronics rack.

a homogeneous distribution of similarly orientated regions of grains (bi-modal) across the billet cross-section. Image B again shows a homogeneous distribution; however, in this case the similarly orientated regions are finer. This is due to small changes in the chemical composition of the material altered to refine the macrostructure. The inset zooms show the difference in the microstructure between the two materials more clearly. These images would have taken  $\sim 8\frac{1}{2}$  days to obtain with the previous generation instrument.

The size of sample that can be scanned is limited only by the scanning method, either the range of the scanning stages (in our case  $300 \times 300 \text{ mm}^2$ ) or the range of motion of the scanning head.

## 4. Spatial and velocity resolution

### 4.1. Spatial resolution

The spatial resolution of the SRAS instrument is adjustable by making minor changes to the optics, for example, changing

the objective lens or the size of the mask aperture. The spatial resolution differs with direction as shown in figure 5.

The orthogonal spatial resolution ( $O_{\text{res}}$ , the direction perpendicular to the projected grating direction, see figure 5) depends predominantly on the size of the optical spot and the spacing from the pattern (this assumes the vertical projection size is larger than the probe beam spot size and the distance of the probe from the patch). The orthogonal resolution is related to where on the generation patch the signal reaching the probe beam originated. For a homogenous sample, this depends on the probe spot size and the diffraction of the acoustic waves; for a multigrain sample, the different grains aberrate the acoustic wave front such that the acoustic energy is redistributed in different regions as it propagates; this means that for a particular point on the sample the acoustic energy could have come from different parts of the generation patch. Reducing the number of grain boundaries between the generation and detection spot reduces this effect but keeping the detection spot in the near field. In general, the orthogonal resolution

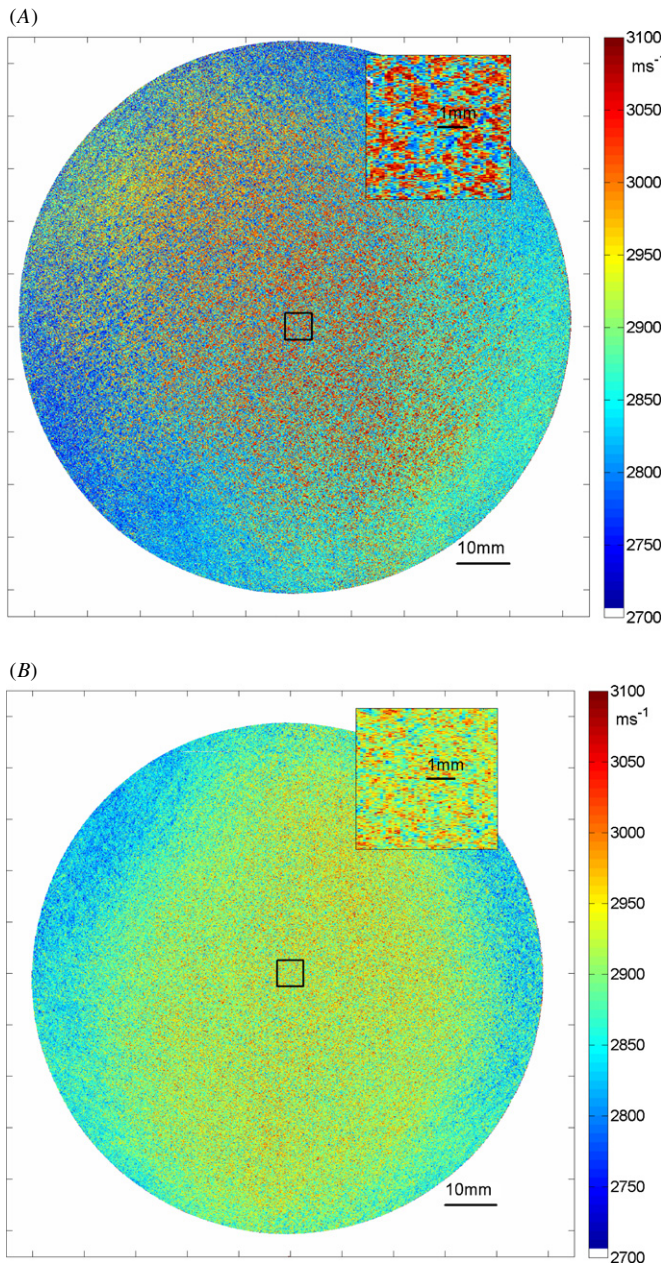


**Figure 4.** 7.5 megapixel high-resolution images of Ti6Al4V alloy where slight changes to the manufacturing process lead to different grain structures shown in (A) and (B).

is much smaller than the parallel resolution and is typically around  $20\ \mu\text{m}$  (for a  $200\ \mu\text{m}$  patch size).

The parallel resolution ( $P_{\text{res}}$ ) is related to the patch size directly, the expected edge response is the convolution of a top hat function (the hard edge aperture of the system) and the sharp edge at a grain boundary. This gives a smooth transition from one region to the other where the width of the transition is the patch size.

However, in SRAS images the edges often appear very sharp; this is a result of the nonlinear processing that is performed. Figure 6 shows a transition between two grains on a titanium sample, the left shows the transition for a  $600\ \mu\text{m}$  patch, the transition from blue to yellow is sharp, for the

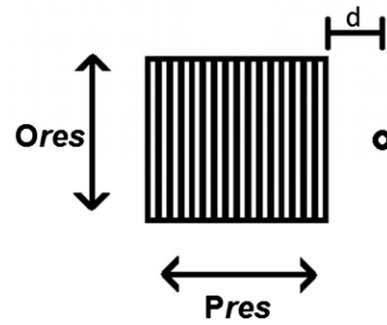


**Figure 5.** Cartoon showing the orthogonal and parallel directions—the spatial resolution in each direction depends on different factors.

$120\ \mu\text{m}$  patch the transition is much smoother (the transition width is approximately the size of the patch size as expected). How the edge *appears* in an image depends on several factors: the SNR of the measurement, the velocity difference between the two grains, the generation efficiency for each wave (which will be different for different grain orientations), the patch size and the processing method.

To look at this in more detail, we have used a simple model of the system to see how the SRAS processing affects how the edges look in the final image. Figure 7(a) shows a simulated transition across a grain boundary edge for one patch size. The SRAS processing method used finds the peak of the FFT for the weighted sum of two frequency components corresponding to the amount of the patch on each side of the transition.

In this case at the boundary edge, we see the reduction of one frequency component and the increase of the other frequency. The SRAS processing method (by looking for the peak of the FFT) is nonlinear and so this leads to ‘hard’ edges in the images as the returned velocity flips from one velocity value to another (the overlaid stars are the selected velocity value). This can give the impression that the spatial resolution is higher than it really is, as shown in figure 7(b) where the edge responses appear much sharper (green is true edge response, blue is the recovered edge response). If the velocity difference is small so that the two peaks are not distinct, then the edge response is as expected. (figures 7(c) and (d)).

If the velocity difference is small, then the peaks from the two regions are not resolved; therefore, the peak of the FFT is simply the weighted average of the contributions from each region; this produces an edge response that is continuous with the transition width and related to the excitation patch size.

The practical limit to the achievable spatial resolution is governed by the optical diffraction limit and the number of fringes that are needed to be projected onto the sample to obtain an acceptable velocity resolution.

#### 4.2. Velocity resolution

The velocity resolution is determined by the number of lines in the generation patch. The more the lines that are present, the sharper the peak in the frequency domain, increasing the signal to noise ratio (SNR) of the measured velocity.

If we consider two cases, one where the generation laser power is limited, such that to increase the number of projected

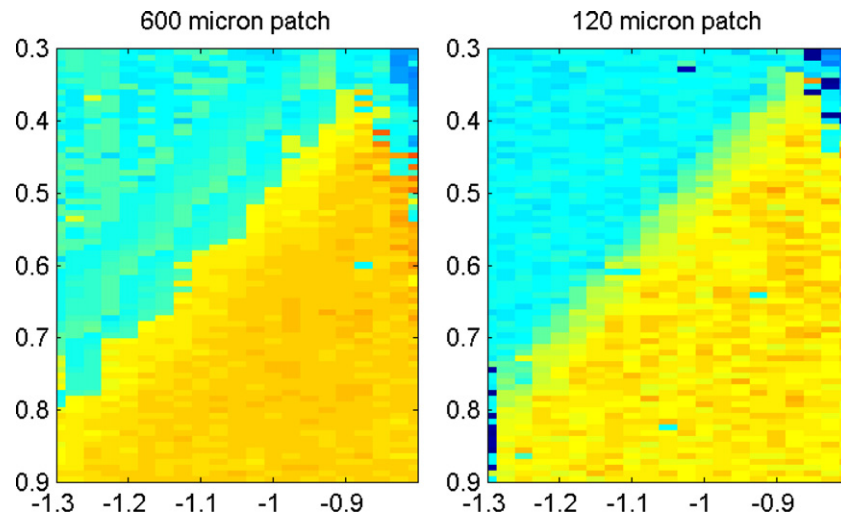


**Figure 6.** SRAS image of an edge with two different patch sizes; the large patch has a much sharper transition even though the resolution is lower.

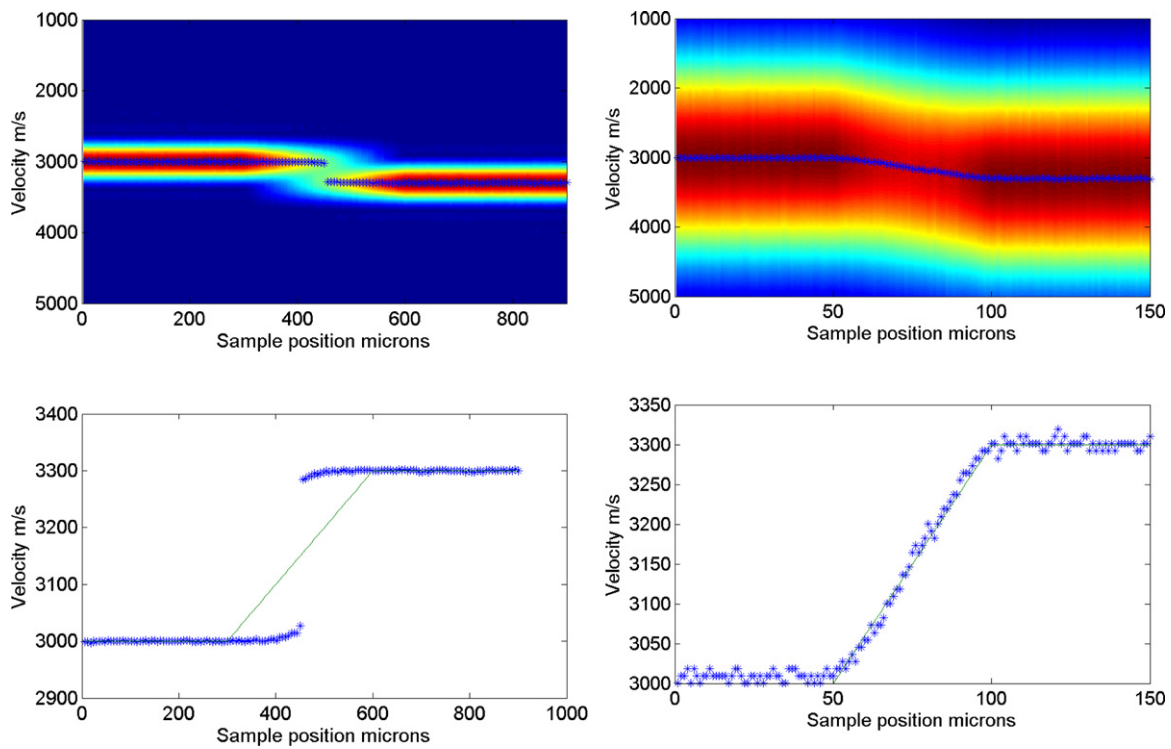


**Figure 7.** (a) Simulated velocity as a grain boundary is crossed; the component at  $3000 \text{ m s}^{-1}$  reduces as the  $3300 \text{ m s}^{-1}$  component increases. The stars show the velocity chosen by the processing algorithm. (b)  $50 \mu\text{m}$  patch size; the smaller patch has a broader frequency response and so the two components are not easily separable. (c) and (d) The recovered edge response in blue and the actual edge response in green. For the smaller patch, the edge response is as expected but for the large patch the edge response appears much sharper.

lines requires the spreading out the laser energy over a larger area, and one where the sample damage threshold limits the generation, then we can calculate the impact of increasing the number of fringes on the error of the velocity measurement.

**4.2.1. Case 1: total power limit.** Using a similar approach to the above to simulate the expected response, assuming a uniform sample and taking different numbers of cycles and weighting the amplitude such that the total energy is the same, we can see how the error in the velocity varies. The noise is

assumed to be dominated by the probe light level and as such does not change for the different generation patch sizes.

Figure 8(a) shows the error in the recovered velocity for different patch sizes. The SNR given is for the smallest patch size. As the patch size is increased, the amplitude of the signal decreases as the energy is spread out over the new patch size and this reduces the SNR for the larger patches, but despite this we see that increasing patch size gives improved velocity resolution.

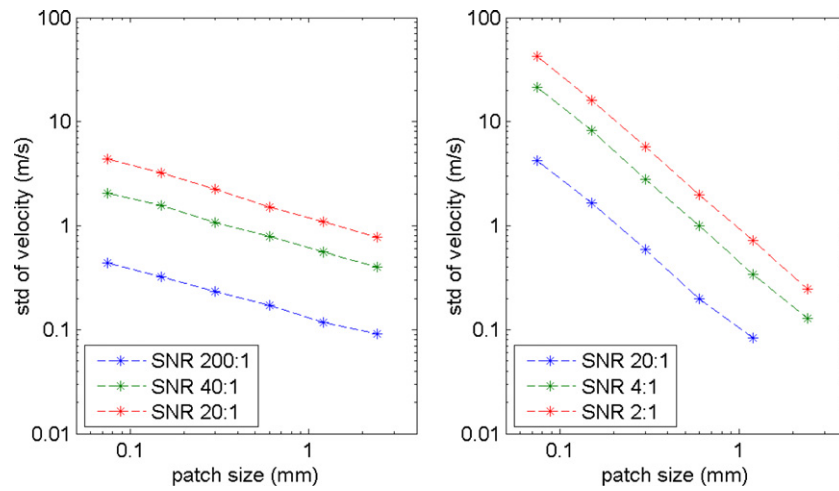


**Figure 8.** (a) Effect of increasing the patch size on velocity resolution when the generation power is fixed; the larger patch size gives better velocity resolution. (b) The case where the sample damage threshold limits the optical power shows even a faster decrease in the velocity error with increasing patch size.

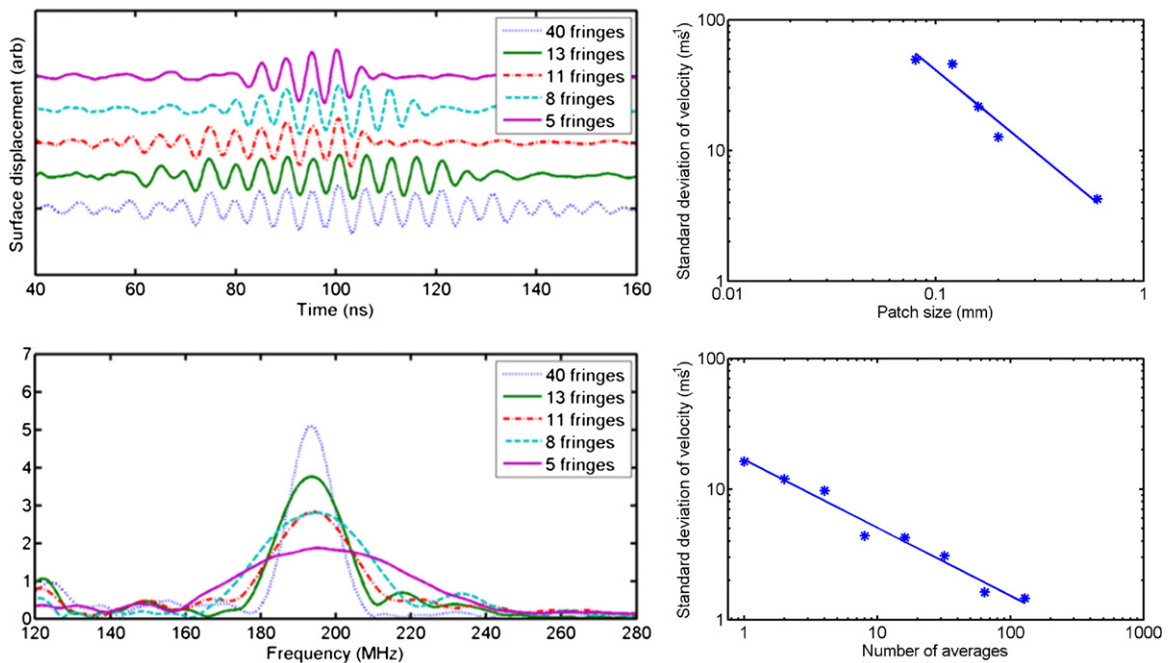


**Figure 9.** (a) Experimental traces for different aperture sizes (number of lines present) and (b) their spectrum showing the smaller patch sizes having lower and wider responses. (c) The influence of the patch size on the averaged velocity resolution—large patch improves the velocity resolution. (d) The reduction in velocity error with averages reducing as  $\sqrt{\text{averages}}$  as expected.

**4.2.2. Case 2: sample damage threshold limit.** Case 1 does not usually occur in practice, as in general we are not limited by the total generation laser power, but by the sample damage threshold. For this case, as we add more lines we add more signal as the amplitude for the added lines remain the same. The results are shown in figure 8(b), where we can see that increasing patch size has an even stronger response in reducing the velocity error: the gradient is  $-1.5$  (compared to  $-0.5$  for the previous case). Here, the SNR figures correspond to the SNR for all the patch sizes.

**4.2.3. Experimental measurements of spatial and velocity measurements.** Figures 9(a) and (b) demonstrate

experimental results showing similar behaviour to the above. By changing the generation patch size whilst keeping the grating period fixed, we see the FWHM of the signal increases and the height decreases as the patch size is reduced.

Figure 9(c) shows the effect of reducing the patch size on the velocity error (128 averages were used to improve the SNR of the smaller patch size data). The gradient is approximately  $-1.5$  as expected from the simulations above.

Figure 9(d) shows the effect this has on the velocity error using a large patch size ( $600 \mu\text{m}$ ); the single shot velocity noise is  $\sim 15 \text{ m s}^{-1}$  (0.5% variation) If averaging is employed, then this reduces with the square root of the number of averages as expected and at 128 averages is  $\sim 1.5 \text{ m s}^{-1}$  (0.05% variation)



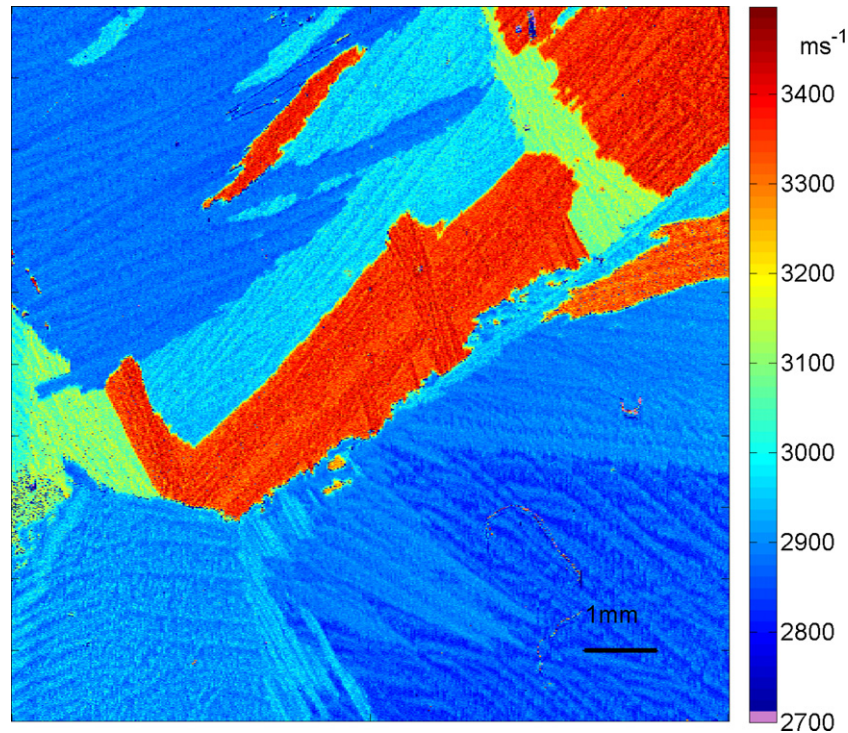


**Figure 10.** Image of TiLG685 showing the internal structure within the large grains, the crystallites are clearly visible, and spatial resolution is  $\sim 50 \mu\text{m}$ .

In practice, for high resolution scans, we limit the number of fringes to a minimum of  $\sim 5$  as this makes the measurement easier to perform as it keeps the bandwidth of the generated frequencies within the working range of the amplifiers and filters used in the electronics chain. For scans where the resolution is less important, we use as many fringes as possible.

The velocity maps in figures 4 were taken using a  $\times 5$  imaging system to produce a generation patch size of around  $200 \mu\text{m}$  giving a spatial resolution of the order of  $100 \mu\text{m}$ . Figure 10 shows a scan of Ti-LG 685 with a  $\times 10$  imaging lens, producing a patch size of  $\sim 100 \mu\text{m}$  and a resolution of around  $50 \mu\text{m}$ . Using the smaller patch size shows many fine details of the crystallites within the larger grain structure.

Using a high NA objective and a small mask size, we could ultimately produce a spatial resolution of around  $5 \mu\text{m}$ ; however, at the moment our detection electronics does not allow us to detect waves of this frequency ( $\sim 3 \text{GHz}$ ) although there is no reason why detectors could not be designed for this frequency range.

## 5. Velocity measurements in more than one propagation direction

Surface velocity maps are very useful for showing material microstructure but a single map cannot identify all grains in a given sample as there may be different grain orientations that produce the same acoustic velocity value for a single propagation direction. To obtain a more complete picture of the material structure, the SAW velocity can be measured in different directions and a composite image produced.

### 5.1. Vector scans

When two orthogonal directions are scanned a velocity vector map can be produced. This is achieved by combining the two SAW velocity maps into a single image with a new colour map. Different colours are chosen depending on the measured velocity in both images, for example if the velocity is fast in both images it is coloured blue, fast and slow is coloured green and slow and fast is assigned red. The velocity vector map identifies most grains in the material as the number of cases where the different grain orientations produce the same measured velocity in orthogonal directions is considerably less than the situation where one direction is only taken.

Some specific orientations can be identified from a vector map, for example, in a hexagonal crystal material, if the velocities are fast and fast in both images the measurement must have taken place close to the basal plane. Fast and slow means the grain lies approximately  $90^\circ$  to the basal plane; slow and fast is orthogonal to this [23]. While this is not exhaustive, it does provide some insight into the texture of material.

Figure 11 shows an example of how two velocity maps taken at  $90^\circ$  are combined into a vector map for a Ti-6Al-4V forging. This material has been processed above the beta transus temperature leading to a fully transformed lamellar microstructure. This lamellar microstructure is clearly visible in the SRAS image and the mis-orientation between neighbouring ‘packets’ is apparent.

### 5.2. From contrast to orientation

To go from velocity maps to orientation maps involves fitting the measured velocity surface for each measured grain to the

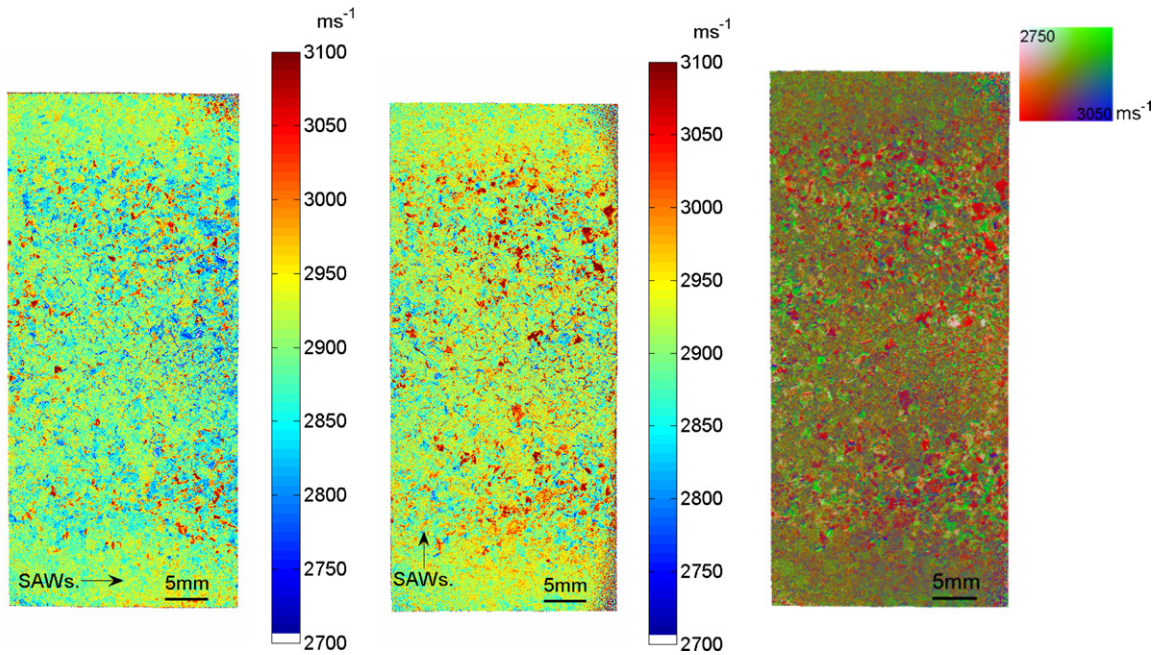


**Figure 11.** Two velocity maps with orthogonal acoustic propagation directions and the composite velocity vector map for a Ti6Al4V sample processed above the beta transus temperature leading to a fully transformed lamellar microstructure.

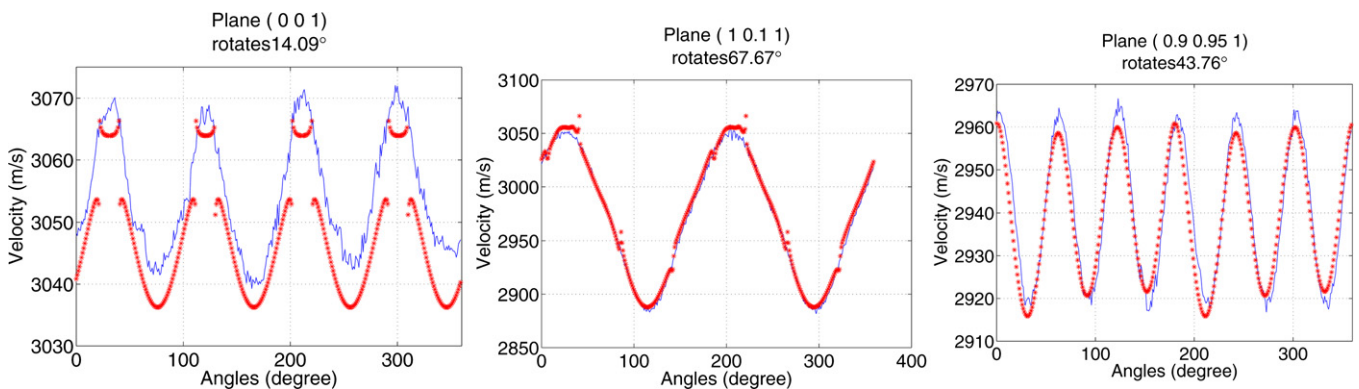


**Figure 12.** Velocity surfaces for three single crystal aluminium samples and the corresponding fitted modelled data.

expected velocity surface calculated from theory. This process is quite involved and so is only explained in brief here; more details are available in [24].

The acoustic velocity of a known material in a known orientation can be calculated analytically. We use the method outlined by Farnell [25]. This method is used to calculate SAW and pseudo-SAW velocities on different crystallographic planes by using iterative search procedures and the material's known elastic constants.

The calculated results need to be modified to take into account the response of the detector. The knife edge detector is sensitive only to the out-of-plane motion of the waves, so we calculate the out-of-plane motion for all of the calculated modes and choose the dominant one. This then gives us an indication of the expected velocity surface for that crystallographic orientation that will be measured with the SRAS instrument.

The inverse problem is difficult to solve directly, so to provide orientation measurements we use the measured velocity surface and fit it to the model data. The fitting

is achieved using cross correlation; we record the strength of the correlation of the experimental data with each plane and rotation in the calculated velocity values database. This exhaustive search is a brute force approach and by no means optimal. At the current time, on a typical desktop PC the fitting process takes approximately 0.1 s per point.

Using this approach, we are able to measure the crystallographic orientation of a material. Figure 12 shows the velocity surfaces measured by SRAS and the obtained plane from the fitting procedure above for several known Al crystal planes. The measured plane obtained from the fitting procedure is very close to the expected plane for these known samples. This shows that the fitting procedure produces accurate results.

The velocity surfaces above were obtained for just a single point on the sample surface, but if we raster scan the sample and take measurements at different angles at each point we can produce an orientation map for the whole sample.

Figure 13 shows a zoom of the velocity maps obtained from the instrument for different propagation angles on a large grained Al sample. These maps are fitted to the calculated

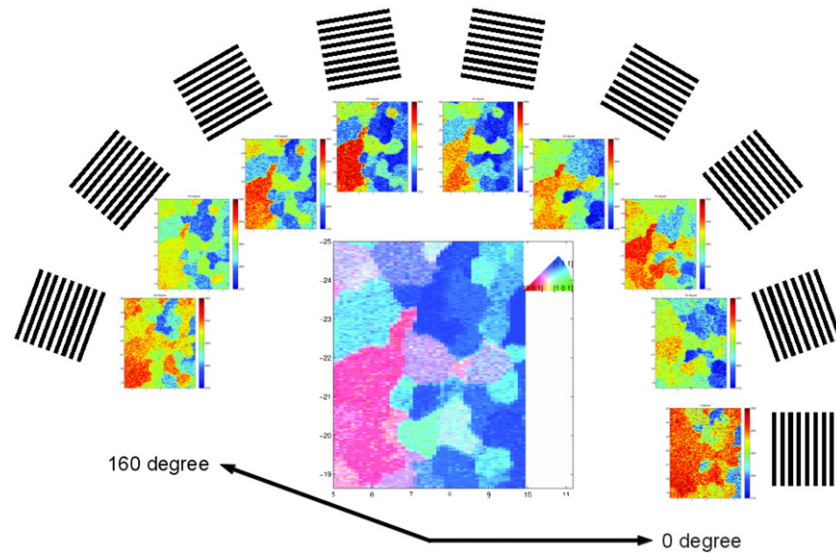


**Figure 13.** Zoomed section of velocity maps for different fringe projection angles and the corresponding orientation map.

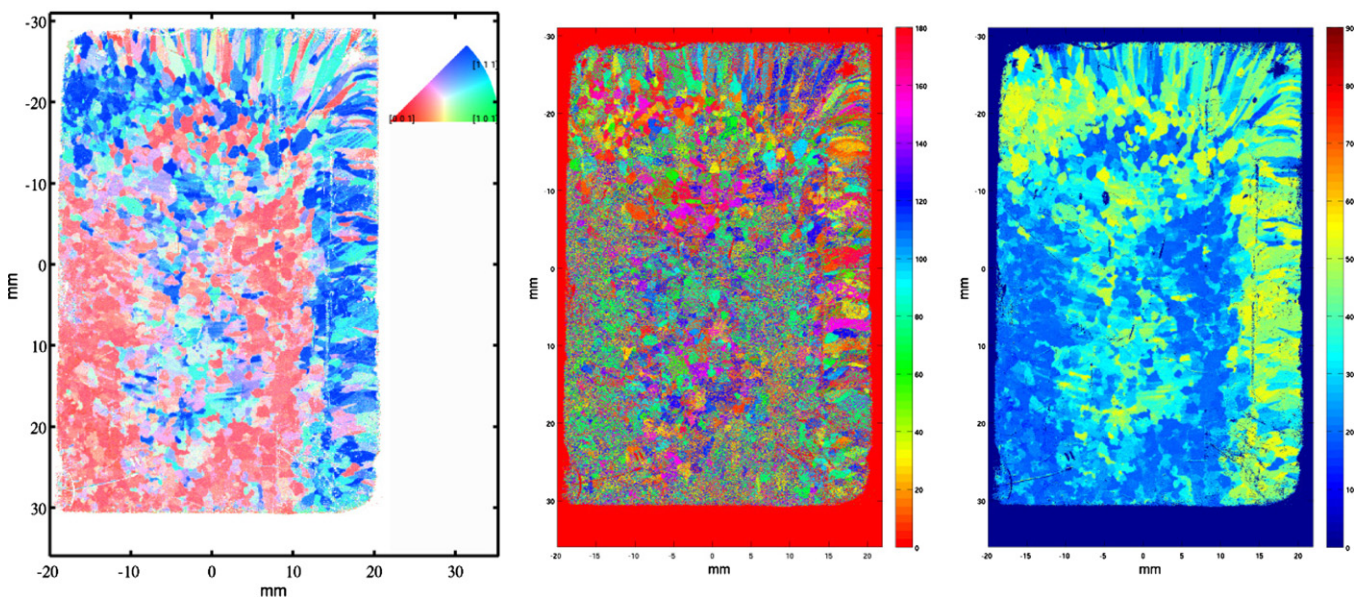


**Figure 14.** (a) Inverse pole figure. (b) The rotation of the plane. (c) Angle to 001 of a large grained Al sample.

velocity database to work out the orientation for each pixel in the image as shown in the centre of the figure.

The end result of this process is shown in figure 14. Figure 14(a) shows the orientation map showing the plane of each grain, (b) shows the angle of rotation of that plane from the vertical and (c) shows the angle to plane 001.

The variation within a single grain is small; taking one of the large blue grains at the edge in the angle to 001 plot, the mean angle is  $\sim 20^\circ$  and the standard deviation is less than  $1.5^\circ$  between different points in the grain showing that the measurement is precise. This is similar to x-ray diffraction (Rvalue standard deviation  $< \pm 1.5^\circ$  [26]), but worse than a typical EBSD system (mis-orientation between grains better than  $0.5^\circ$  [27]). Aluminium is fairly isotropic and so the variation of velocity is relatively small compared to other more anisotropic materials (e.g. nickel, titanium) and so orientation measurements on these materials will be more robust to noise.

## 6. Discussion

The SRAS instrument is a versatile tool for imaging material microstructure; it can be configured for a wide range of spatial and velocity resolutions due to the common objective used for the generation and detection optics allowing rapid switching of generation and detection spot sizes.

The size of the instrument has been significantly reduced from the previous generation machine and is now such that it can easily be transported and mounted on a scanning rig.

The new instrument has high scanning rates, it is 100 times faster than previous generations of SRAS instruments and as it does not require vacuum chambers or scanning samples at angles the sample size is limited only by the sample stages or the scanning rig.

Despite the considerable advancement made with the instrument reported here, there are still some areas where

further development will be beneficial. With additional modifications the scanning head could be made even smaller and lighter to allow it to be mounted on a multi-axis scanning gantry. This would improve the utility of the instrument by enabling the scanning of non-flat surfaces—e.g. real industrial parts.

There is a growing need to provide measurements on parts with little or no surface preparation; as mentioned in the introduction, this is becoming particularly relevant to additive manufactured parts; the challenges for this technique and the potential for SRAS have been considered in [28]. To give the instrument this capability involves replacing the knife edge detector with a rough surface capable detector, for example, a Fabry–Perot interferometer.

## Acknowledgments

We wish to thank the East Midlands Development Agency (now defunct) for funding the construction of this instrument and Matt Thomas at TIMET for providing the titanium samples.

## References

- [1] Savage M W R 2011 The influence of crystal orientation on the elastic stresses of a single crystal nickel-based turbine blade *J. Eng. Gas Turbines Power* **134** 012501
- [2] Arakere N K and Swanson G 2000 Effect of crystal orientation on fatigue failure of single crystal nickel base turbine blade superalloys *J. Eng. Gas Turbines Power* **124** 161–76
- [3] Armstrong R W 1970 The influence of polycrystal grain size on several mechanical properties of materials *Metall. Mater. Trans.* **1** 1169–76
- [4] Berbenni S, Favier V and Berveiller M 2007 Impact of the grain size distribution on the yield stress of heterogeneous materials *Int. J. Plast.* **23** 114–42
- [5] Bache M and Evans W 2001 Impact of texture on mechanical properties in an advanced titanium alloy *Mater. Sci. Eng. A* **319–321** 409–14
- [6] Evans W J and Bache M R 1994 Dwell-sensitive fatigue under biaxial loads in the near-alpha titanium alloy IMI685 *Int. J. Fatigue* **16** 443–52
- [7] Bantounas I, Lindley T C, Rugg D and Dye D 2007 Effect of microtexture on fatigue cracking in Ti–6Al–4V *Acta Mater.* **55** 5655–65
- [8] Dunne F P E, Rugg D and Walker A 2007 Lengthscale-dependent, elastically anisotropic, physically-based hcp crystal plasticity: application to cold-dwell fatigue in Ti alloys *Int. J. Plast.* **23** 1061–83
- [9] Bache M and Tasleem M 1999 Fatigue life prediction techniques for notch geometries in titanium alloys *Int. J. Fatigue* **21** (Suppl. 1) S187–97
- [10] Hertzman S, Brolund B and Ferreira P J 1997 An experimental and theoretical study of heat-affected zone austenite reformation in three duplex stainless steels *Metall. Mater. Trans. A* **28** 277–85
- [11] Knipling K E and Fonda R W 2011 Microstructural evolution in Ti-5111 friction stir welds *Metall. Mater. Trans. A* **42** 2312–22
- [12] Clark D, Whittaker M T and Bache M R 2012 Microstructural characterization of a prototype titanium alloy structure processed via direct laser deposition (DLD) *Metall. Mater. Trans. B* **43** 388–96
- [13] Wang F, Williams S, Colegrove P and Antonysamy A A 2013 Microstructure and mechanical properties of wire and arc additive manufactured Ti-6Al-4V *Metall. Mater. Trans. A* **44** 968–77
- [14] Bourell D L, Leu M C and Rosen D W (ed) 2009 *Roadmap for Additive Manufacturing: Identifying the Future of Freeform Processing* (Austin, TX: The University of Texas at Austin, Laboratory for Freeform Fabrication, Advanced Manufacturing Center) p 9
- [15] Belyakov A, Tsuzaki K, Kimura Y, Kimura Y and Mishima Y 2007 Comparative study on microstructure evolution upon unidirectional and multidirectional cold working in an Fe–15%Cr ferritic alloy *Mater. Sci. Eng. A* **456** 323–31
- [16] Yang D K, Cizek P, Hodgson P D and Wen C E 2010 Microstructure evolution and nanograin formation during shear localization in cold-rolled titanium *Acta Mater.* **58** 4536–48
- [17] Vander Voort G F 1984 *Metallography: Principles and Practice* (New York: McGraw-Hill) pp 166–72
- [18] Gifkins R C 1970 *Optical Microscopy of Metals* (Amsterdam: Elsevier)
- [19] Clay K, Jackson J D, Quedsted P N and Morrell R 2009 Improving single crystal orientation determination for advanced nickel-based alloys *Measurement Good Practice Guide 112* (Teddington, UK: National Physical Laboratory) p 112
- [20] Randle V 2003 *Microtexture Determination and Its Applications* (London: Maney Publishing)
- [21] Sharples S D, Clark M and Somekh MG 2006 Spatially resolved acoustic spectroscopy (SRAS) for fast noncontact imaging of material microstructure *Opt. Express* **14** 10435–40
- [22] Scruby C B and Drain L E 1990 *Laser Ultrasonics: Techniques and Applications* (London: Taylor and Francis)
- [23] Royer D and Dieulesaint E 1984 Rayleigh wave velocity and displacement in orthorhombic, tetragonal, hexagonal, and cubic crystals *J. Acoust. Soc. Am.* **76** 1438–44
- [24] Li W, Sharples S, Smith R, Clark M and Somekh M 2012 Determination of crystallographic orientation of large grain metals with surface acoustic waves *J. Acoust. Soc. Am.* **132** 738–45
- [25] Farnell G W 1970 *Properties of Elastic Surface Waves (Physical Acoustics)* vol 6 ed W P Mason and R N Thurston (New York: Academic) pp 109–66 chapter 3
- [26] Clay K, Mingard K, Morrell R and Quedsted P 2010 R value measurement issues for grain boundaries in nickel single crystal castings *Mater. Sci. Technol.* **26** 781–6
- [27] Trimby P, Day A, Mehnert K and Schmidt N-H 2002 Is fast mapping good mapping? A review of the benefits of high-speed orientation mapping using electron backscatter diffraction *J. Microsc.* **205** 259–69
- [28] Clark D, Sharples S D and Wright D C 2011 Development of online inspection for additive manufacturing products *Insight Non-Destr. Test. Cond. Monit.* **53** 610–3